ELSEVIER

Fabrication and characterization of cerium-doped barium titanate inverse opal by sol–gel method

Yi Jin[a], Yihua Zhu[a],*, Xiaoling Yang[a], Chunzhong Li[a], Jinghong Zhou[b]

[a]*Key Laboratory for Ultrafine Materials of Ministry of Education, School of Materials, Science and Engineering, East China University of Science and Technology, Shanghai 200237, PR China*
[b]*UNILAB, State Key Laboratory of Chemical Engineering, East China University of Science and Technology, Shanghai 200237, PR China*

Abstract

Cerium-doped barium titanate inverted opal was synthesized from barium acetate contained cerous acetate and tetrabutyl titanate in the interstitial spaces of a polystyrene (PS) opal. This procedure involves infiltration of precursors into the interstices of the PS opal template followed by hydrolytic polycondensation of the precursors to amorphous barium titanate and removal of the PS opal by calcination. The morphologies of opal and inverse opal were characterized by scanning electron microscope (SEM). The pores were characterized by mercury intrusion porosimetry (MIP). X-ray photoelectron spectroscopy (XPS) investigation showed the doping structure of cerium, barium and titanium. And powder X-ray diffraction allows one to observe the influence of doping degree on the grain size. The lattice parameters, crystal size and lattice strain were calculated by the Rietveld refinement method. The synthesis of cerium-doped barium titanate inverted opals provides an opportunity to electrically and optically engineer the photonic band structure and the possibility of developing tunable three-dimensional photonic crystal devices.
© 2006 Elsevier Inc. All rights reserved.

Keywords: Photonic crystal; Barium titanate; Cerium; Dope; Inverse opal

1. Introduction

Three-dimensional photonic crystals (3D PCs) represent a new class of materials that can function as "semiconductors for light" [1,2]. The defining feature of a 3D PC is the periodicity of the dielectric constant along all three spatial dimensions and the unique ability of 3D PCs to control the flow of photons originates from total or partial suppression of the photon density of states (DOS) for certain wavelengths.

Self-assembly of monodisperse colloidal spheres provides an alternative fabrication of photonic crystals [3–6]. Polymer latexes, the most studied and best-established examples of monodisperse colloidal spheres are employed as the building blocks of photonic crystals. There are a number of reasons for choosing monodispersed colloidal spheres as the building blocks to fabricate photonic crystals. Most theoretical models (e.g., the Mie theory [7] that deal with the properties of colloidal particles and the interactions between them are usually based on the spherical shape. In principle, the intrinsic properties of monodisperse colloidal spheres can be tightly controlled by changing the parameters: (i) the diameter; (ii) the chemical composition; (iii) the bulk substructure; (iv) the crystallinity (polycrystalline, single crystalline, or amorphous); and (v) the surface functional group (thus the interfacial free energy and surface charge density). The sphere may also represent the simplest form that a colloidal particle can easily adopt during the nucleation or growth process, as driven by minimization of interfacial energy [8].

Because inverted opals with diverse compositions are considered to be with better optical properties, and can be formed by infiltrating nanochannels of the opal structure [9–11], they have been synthesized by replicating the interstitial structure of silica or polystyrene (PS) opals.

*Corresponding author. Fax: +86 21 64250624.
E-mail address: yhzhu@ecust.edu.cn (Y. Zhu).

Examples of synthetic inverted opals include metals [12], semiconductors [13–15], oxides [16], and conducting polymers [17].

$BaTiO_3$ is one of the especially useful materials in the microelectronics industry. Because of its high dielectric constant, $BaTiO_3$ can be used as substrate and insulating layers in solid state displays and flat panel displays based on electroluminescent and photochromic effects. And doped $BaTiO_3$ materials have extensive uses, such as $(Ba,Sr)TiO_3$ (BST) ceramics are widely used in capacitors and BST thin films are useful for making tunable microwave components, random access memories (RAM), and infrared detectors [18]. Besides cerium-containing materials show a wide range of remarkable properties, which make them essential to a large variety of current applications [19], these include integrated-optical devices, laser glasses, fluorescent lamps, phosphors, and many others [20,21]. Just like silicon, $Ce:BaTiO_3$ is very suitable for the dynamic research due to its high index of refraction, fast time response and weak absorption in the visible and near infrared region [22].

For this purpose, we report the fabrication of three dimensional cerium-doped $BaTiO_3$ inverted opal, which is expected to be an advanced and promising applications, such as a new application of the all-optical switching or reversible recording medium for real-time holography due to its fast photorefractive effect [23].

2. Experimental section

2.1. Synthesis of polystyrene nanoparticles

The positively charged, cross-linked PS particles (diameter ~330 nm) were prepared by emulsion polymerization of styrene monomer (60 mL) at 75 °C for 4 h using sodium dodecyl sulfonate (0.4 g) as the surfactant and ammonium persulfate (0.75 g) as the initiator [24].

2.2. Synthesis of Ce-doped $BaTiO_3$ precursor

In a typical reaction, 3.063 g (12.59 mmol) of $Ba(OAC)_2$ was dissolved in 5 mL of acetic acid, refluxed at 70 °C for ~20 min. The $Ce(OAc)_3$ (Ce: Ba mol ratio is 0.05: 0.95, 0.07: 0.93 and 0.10: 0.90 as sample 1, 2 and 3, respectively) mixed with 5 mL acetate acid was added to the $Ba(OAC)_2$ solution. The mixed solution was magnetic stirred for 1 h, and then allowed to cool to room temperature. A second solution of $Ti[O(CH_2)_3CH_3]_4$ (13.22 mmol of sample 1, 13.47 mmol of sample 2 and 13.85 mmol of sample 3) and 2.5 mL of ethanol was prepared and added to the $Ba(OAC)_2$ solution with magnetic stirred leading to the formation of a clear sol.

2.3. Synthetic method of inverted opal

Fig. 1 illustrates the scheme for the preparation of Ce-doped $BaTiO_3$ inverse opal. PS colloid particles were first
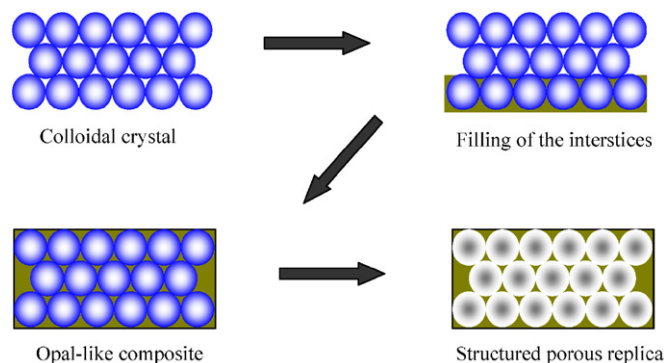

Fig. 1. Schematic illustration of the fabrication of Ce-doped $BaTiO_3$ inverse opal.

crystallized on microslide by an evaporation–sedimentation method adapted from the approach described by Colvin [25] and Nagayama [26]. A typical process is that solution of latex spheres in a water/ethanol mixture (about 10% water in ethanol) was placed in a beaker with a glass slide or silicon substrate positioned vertically in the center at 45 °C. As the water/ethanol mixture evaporated, capillary forces pulled the spheres together to form a well-ordered multi-layer opal crystal on the substrate surface, after two days a 5 cm^2 substrate was covered by an opal film and displayed bright iridescence due to Bragg diffraction. Then the latex opal film was dipped into the precursor solutions and vacuumed for 15 min, then dried for 24 h at room temperature. The cycle of penetration and drying is repeated 3 or 4 times to ensure that the voids in the template were sufficiently filled, and calcined for powder samples.

2.4. Characteristics

Scanning electron microscopy (SEM, JSM-6360LV) was used to characterize the inverse opal film. The pore distribution of the film was used by Surface Area and Porosimetry System (ASAP 2010N). Thermo gravimetric analysis (TGA) (NETZSCH DSC 204) was used to measure the polymer decomposition temperature. It was analyzed under a heating rate of 10 K/min from room temperature to 800 °C and dynamic nitrogen flow of 50 cm^3/min. X-ray powder diffraction (XRD) was carried out using a Rigaku D/max 2550 VB/PC diffratometer with monochromated copper radiation (Cu$K\alpha$, 1.54056 Å). Intensities were obtained in the 2θ range between 20° and 80° with a step of 0.02°. The structure determination and the calculation of the unit cell parameters were performed by Rietveld refinement [27]. The refinement of the structures was carried out with the MATSTUDIO package, developed by Accelrys [28], from XRD data. X-ray photoelectron spectroscopy (XPS) analyses of the samples were performed on a Perkin–Elmer PHI 5000C XPS system with a monochromatic Mg$K\alpha$ source and a charge neutralizer. All the binding energies were referenced

to C 1s peak at 284.6 eV of the surface adventitious carbon. The amount of Ce was quantitatively detected by ICP-AES (IRIS 1000).

3. Results and discussion

The self-organization of microspheres relies on the fact that the face-centered cubic structure (FCC) is low potential structure regarding the mechanical potential energy. Thus, they are stable and likely to arise from the sedimentation of a colloidal suspension of monodisperse microspheres. In this work, the PS spheres with diameter about 330 nm were deposited to an FCC structure by evaporation–sedimentation method. Fig. 2(a) is the top view of the colloid crystal array (CCA) film, and (b) shows the morphology of a fractured section of the same sample. The hexagonal array structures were found for large domains in the sample. In some places of the sample, intermediate structures were observed showing square symmetry, which could be assigned to the (100) plane of the FCC. The thickness (the number of layers) of the CCA film may be controlled by the amount of suspension, the colloidal concentration, and the particle size. The porous distribution was investigated by the mercury intrusion porosimetry (MIP) [29]. In this experiment, the Hg is pumped through the sample from normal pressure to 30000 psi to measure the Hg intrusion. From Fig. 3, we can observe that two types of pore openings are present, which are tetrahedral and octahedral, and the peak of O (octagon) is much stronger than that of T (tetragon). The positions of the peaks match closely with those expected for O and T interstices sites calculated from radius ratio rules. The narrow peak of cumulative intrusion vs. pore size graph and the abrupt up line of incremental intrusion vs. pore size graph from MIP show the pores are monodispersed. The porous distribution was investigated by the MIP. The cumulative and incremental intrusion was plotted against pore diameter and the results are presented in Fig. 3. The narrow peak of cumulative intrusion vs. pore size graph and the abrupt up line of incremental intrusion

vs. pore size graph from MIP show the pores are monodisperse. The average pore diameter and the porosity obtained from Fig. 3 are 32.65% and 55.2 nm, respectively.

Fig. 4 is the scanning electron microscope (SEM) image of the PS opal after infiltrated by Ce-doped $BaTiO_3$ sol–gel. Before infiltrating the PS opal was put into a heater for 2 h at 80 °C. The sintering process endows the opals with mechanical stability and connects every sphere with its neighbors; the success of the inverse opal fabrication strongly depends on the connectivity between PS particles provided by the sintering process [30]. From Fig. 4, we can see that the CCA film still kept an FCC structure after infiltrated.

TGA experiments in Fig. 5 have revealed that all latex was removed at a temperature of 450 °C. Thus, the temperature of 750 °C used to complete the reaction to crystallized $BaTiO_3$ is certainly sufficient to remove the template and obtain inverse opal. The observation of fully decomposing of the polymer at 450 °C agrees well with DSC experiments that reveal an endothermic peak at 404 °C.
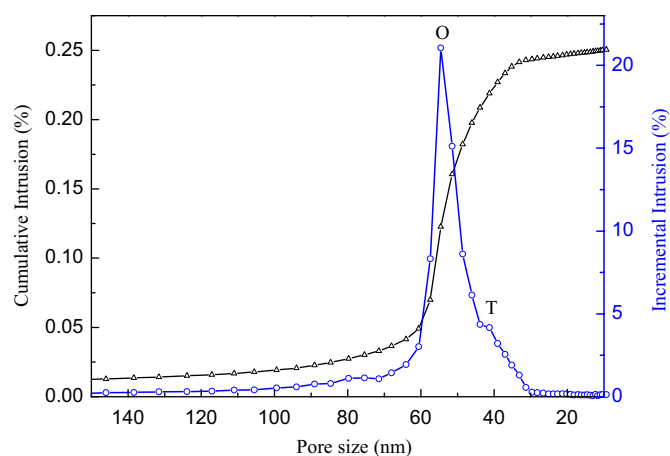

Fig. 3. Mercury intrusion porosimetry (MIP) of PS opal. O: octahedral; T: tetrahedral interstices sites.
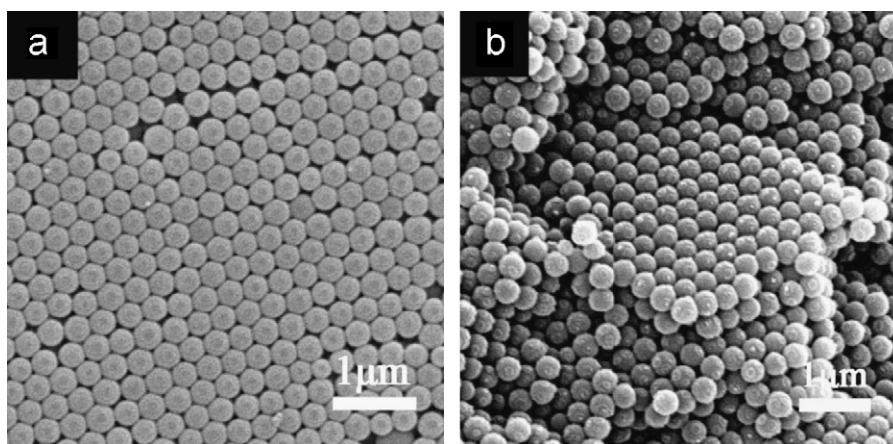

Fig. 2. SEM images of the sample of opal made of ~330 nm spheres: (a) Top view of the PC film in ⟨111⟩ growth direction. (b) Cleaved-edge plane of PS colloidal crystal.
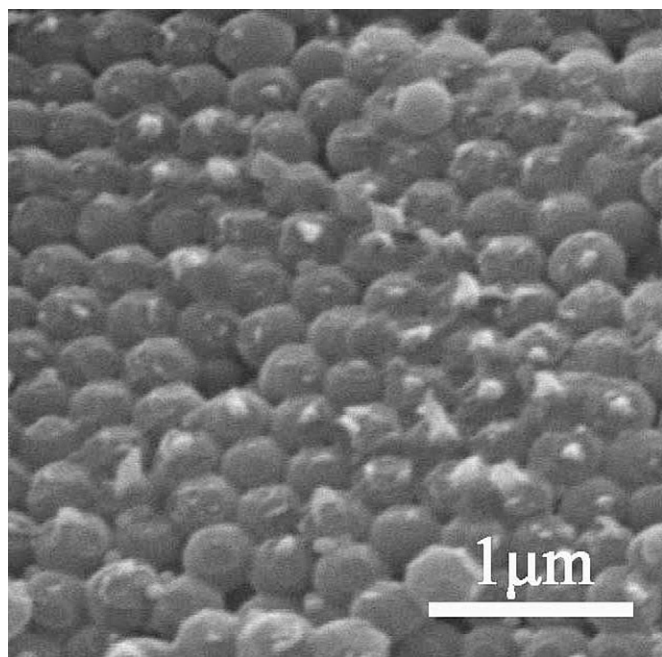
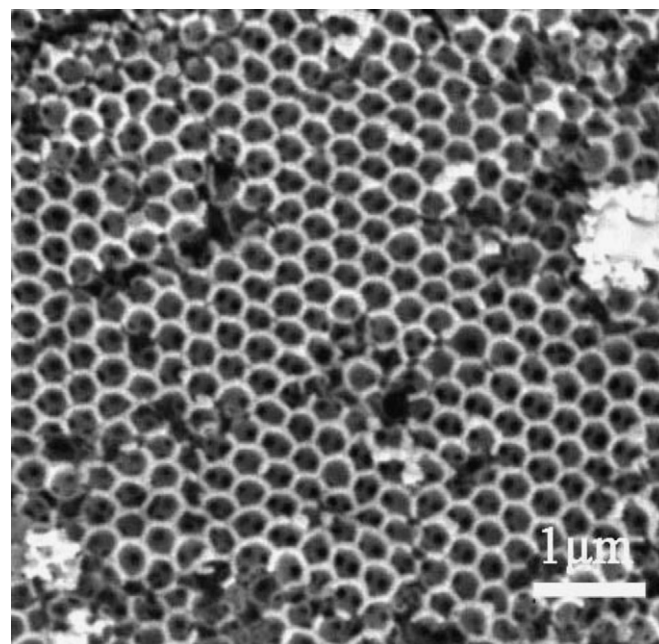Fig. 4. Latex opal infiltrated with Ce-doped BaTiO$_3$ precursor solution.

Fig. 6. SEM image of Ce-doped BaTiO$_3$ inverted-opal, which shows the inverted opal is FCC packed.
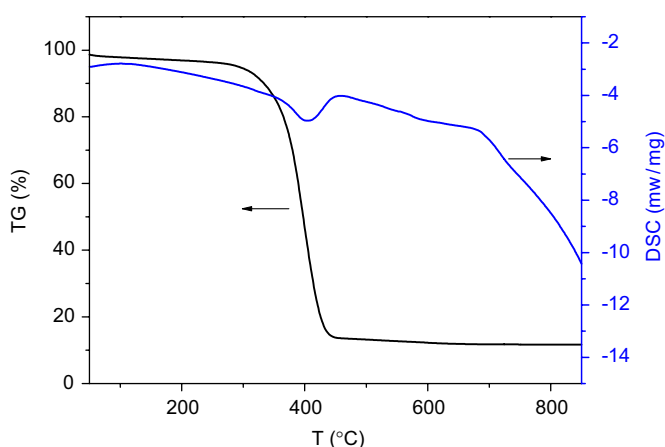

Fig. 5. TG-DSC curve of Ce-doped BaTiO$_3$ inverse opal.

The creation of inverse opal can be simply obtained using very well-established sol–gel chemistry, which the sol–gel precursor solutions infiltrated into the interstitial space of CCA film, and the calcination is the common method for the preparation of inorganic porous materials made with organic templates. Fig. 6 shows the short-range order presented in a Ce-doped BaTiO$_3$ inverted opal sintered at 750 °C. The ordered hexagonal array is observed. The holes connecting the pores are clearly visible and indicate the three-dimensional ordering of the structure of both the inverse opal and CCA film. These holes are important to allow for complete removal of the template through burnout. The defects in Fig. 6 were caused by cracking during the calcination.

The XPS survey spectrums of the sample 2 after calcination are showed in Fig. 7. The XPS peaks (Fig. 7a) illustrate that the particles contain only Ti, Ba, O, and Ce and a trace amount of carbon. No other element is detected. The binding energies of Ti 2p$_{3/2}$, Ba 3d$_{5/2}$ and O 1 s are 457.8, 781.1, and 532.5 eV, respectively. It is known that the line shapes for the Ce(III) and Ce(IV) are different, and the interpretation of cerium spectra is very complex, particularly if mixed oxidation states are present. Ce(IV) exhibits a strong satellite peak near 916.0 eV, whereas Ce(III) compounds do not [31]. And Ce(IV) should enter the BaTiO$_3$ lattice at octahedrally coordinated Ti sites, while Ce(III) in its oxidation state should exchange with dodencahedrally coordinated Ba ions [32]. Fig. 7b showed a position (BE Ce 3d$_{5/2}$ = 884.2 eV) and a band-shape typical for Ce(III) species. The presence of Ce(IV) ions was excluded since no strong peaks around 916.0 eV, typical of tetravalent cerium species, were observed [33]. Ba element corresponds to Ba(II), and Ti element corresponds to Ti(IV). No Ti(III) is detected according to the Ti 2p spectra (see Fig. 7c). Thus, the solid powder may be of the form Ba(II)$_{1-x}$Ce(III)$_x$Ti(IV)O$_{3-x/2}$. The C element is ascribed to the residual carbon from the adventitious hydrocarbon that is often observed in other samples.

Fig. 8 exhibits the experimental X-ray diffraction pattern for the three samples calcinated at 750 °C. The patterns show the cubic phase as the major phase, and no other phase is found, which illustrates that the doping degree is suitable and the three doping degree cannot give rise to the change of the crystal phase. There is little difference of the peaks in the XRD spectrum between the three samples; hence, the Rietveld refinement technique, which is a convenient and a universal method for extracting general information about the structure of nanomaterials, was used to analyze the XRD patterns. The Rietveld refinement
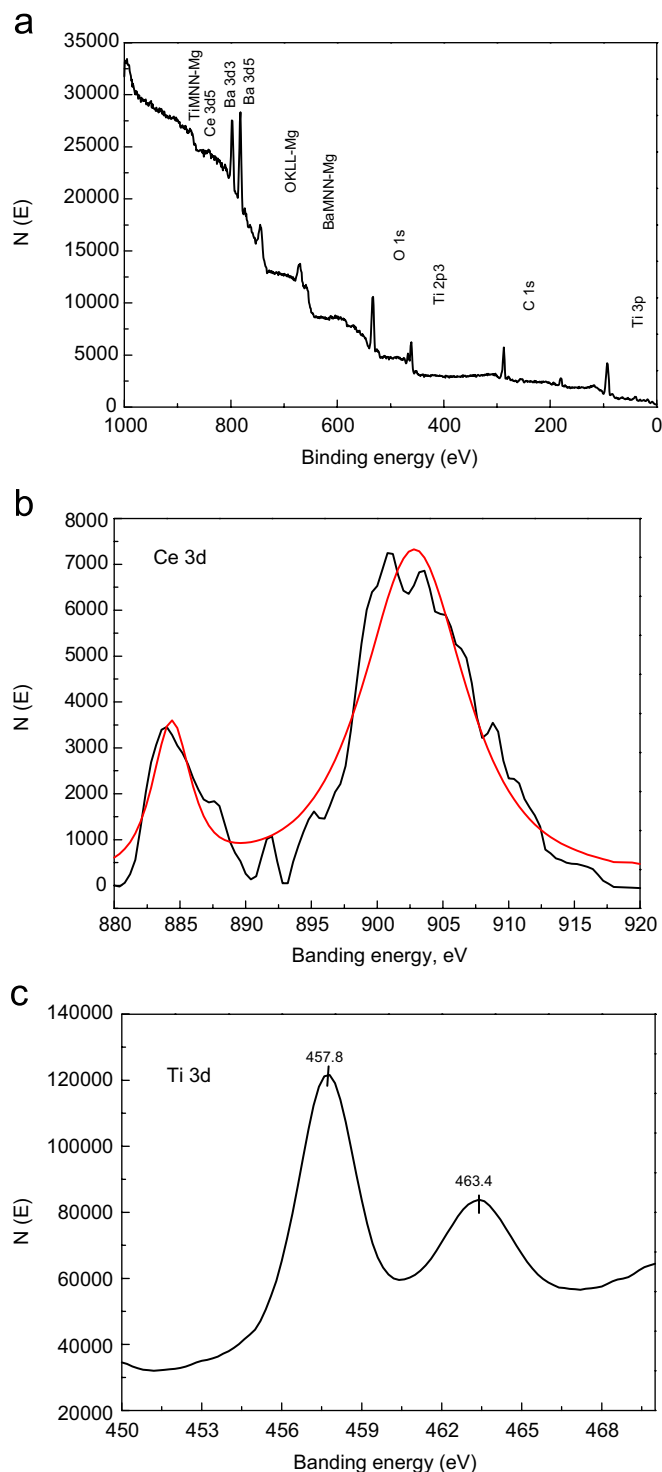
Fig. 8. XRD patterns of Ce-doped $BaTiO_3$ inverse opal with different Ce-doping degree: (a) Ce: Ba = 0.04: 0.96 (sample 1), (b) Ce: Ba = 0.06: 0.94 (sample 2), (c) Ce: Ba = 0.08: 0.92 (sample 3). The calcination temperature was 750 °C.

doping to the lattice parameter between them. The characteristic crystallographic data are collected in Table 1, from which we can see that the real Ce-doping degree quantitatively detected by ICP-AES are lower than the amount added at the beginning. According to these values the lattice strain calculated by Rietveld refinement increased from 0.022 to 0.133 nm and the lattice parameters decrease from 0.40082 to 0.40045 nm with the increasing of Ce-doping degree, which mean that small radius Ce ions substitute for Ba site rather than Ti site. This result is in good agreement with that for the Ba/Ti < 1, it enters on the Ba site substituting for Ba(II) [35,36]. The crystal size is strongly affected by various factors, such as preparation technique, calcinations' temperature and chemical composition. From Table 1, we can see that the crystal size increased from 23.36 to 34.63 nm with the increase of Ce-doping degree. And the three samples' R_{wp} is 15.85%, 16.24% and 14.57%, respectively, which are within limits of error. The final Rietveld plot for sample 3, shown as representative, is given in Fig. 9. A comparison of the observed and the calculated pattern for the sample displayed in the lower trace of Fig. 9 shows good agreement in the range of diffraction angles between 20° and 80°.

4. Conclusion

Ce-doped $BaTiO_3$ inverted opals have been synthesized by a latex opal templating procedure. The as-synthesized Ce-doped $BaTiO_3$ inverse opal has an FCC structure and contains amorphous phase that can be crystallized at 750 °C growing nanocrystals of sufficient size to stabilize the cubic $BaTiO_3$ phase. Structure characterizations by XPS show that Ce element corresponds to Ce(III) substituted for Ba(II) site, and Ba element corresponds to Ba(II), Ti element corresponds to Ti(IV). Rietveld

Fig. 7. XPS survey spectrum (a), Ce 3d XPS spectrum (b) and Ti 2p XPS spectrum (c) of sample 2.

requires a structural model that has an approximation for the actual structure. The starting structural model for the cubic crystal system was built with crystallographic data reported by Buttner and Maslen [34]. Three samples with different doping degree were calculated by Rietveld refinement method to compare the influence of cerium
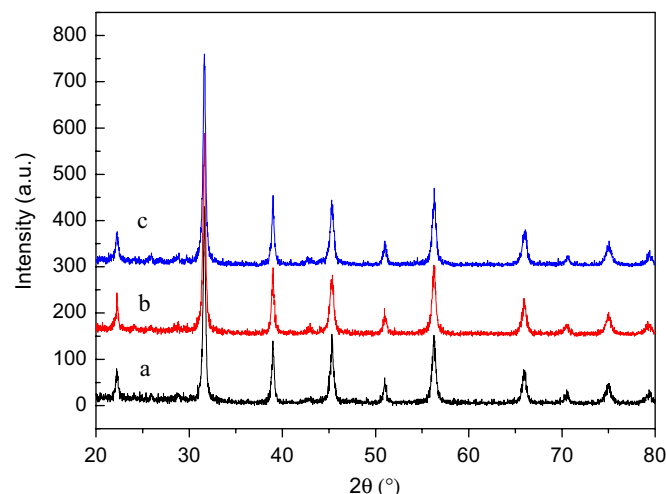
Table 1
Structural parameters and Rietveld agreement factors for samples 1–3

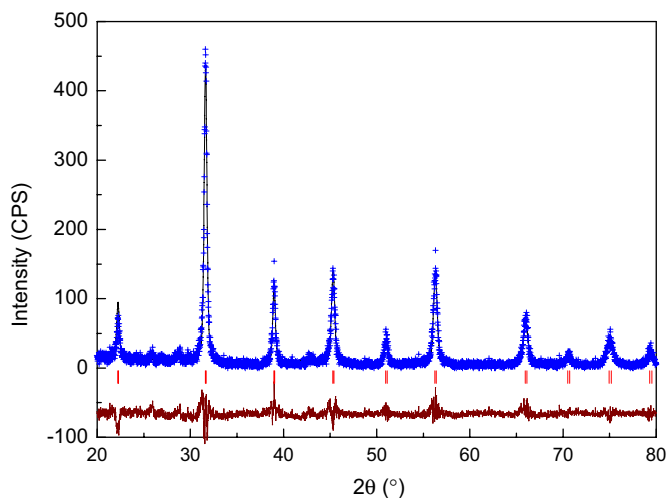| Samples	Atomic ratio Ce/Ba	Lattice para (nm)	Crystal size (nm)	Lattice strain	Final R_{wp} (%)
1	0.04: 0.96	0.40082	23.36	0.022	15.85
2	0.06: 0.94	0.40079	22.73	0.023	16.24
3	0.08: 0.92	0.40045	34.63	0.133	14.57

Fig. 9. Rietveld refinement pattern for sample 3. X-ray data are shown as plus marks; the solid line is the best fit to the data and the tick marks show the positions for the allowed reflections. The lower curve represents the difference between the observed and calculated profiles.

refinement calculation and XRD spectrum characterized the lattice parameter, crystal size and lattice strain. A good match between the calculation and experiment was obtained, which shows the doping degree was suitable. The optical properties are under studied in our further work.

Acknowledgments

References

[1] S. John, Phys. Rev. Lett. 58 (1987) 2486.
[2] E. Yablonovitch, Phys. Rev. Lett. 58 (1987) 2059.
[3] D.S. Raimundo, W.J. Salcedo, Phys. Stat. Sol. B 240 (2003) 124.
[4] F. Caruso, M. Spasova, A. Susha, M. Giersig, R.A. Caruso, Chem. Mater. 13 (2001) 109.
[5] P. Schuetz, F. Caruso, Chem. Mater. 16 (2004) 3066.
[6] X. Xu, G. Friedman, K.D. Humfeld, S.A. Majetich, S.A. Asher, Chem. Mater. 14 (2002) 1249.
[7] G. Mie, Ann. Phys. (Leipzig) 25 (1908) 377.
[8] E. Matijestic, Chem. Mater. 5 (1993) 412.
[9] Y.W. Chung, I.C. Leu, J.H. Lee, M.H. Hon, J. Cryst. Growth 275 (2005) e2389.
[10] N. Matsuura, S. Yang, P. Sun, H.E. Ruda, Appl. Phys. A 81 (2005) 379.
[11] P. Harkins, D. Eustace, J. Gallagher, D.W. McComb, J. Mater. Chem. 12 (2002) 1247.
[12] K.M. Kulinowski, P. Jiang, H. Vaswani, V.L. Colvin, Adv. Mater. 12 (2000) 833.
[13] A. Blanco, E. Chomski, S. Grabtchak, M. Ibisate, S. John, S.W. Leonard, C. Lopez, F. Meseguer, H. Miguez, J.P. Mondia, G.A. Ozin, O. Toader, H.M. van Driel, Nature 405 (2000) 437.
[14] H. Miguez, E. Chomski, F. Garcia-Santamaria, M. Ibisate, S. John, C. Lopez, F. Meseguer, J.P. Mondia, G.A. Ozin, O. Toader, H.M. van Driel, Adv. Mater. 13 (2001) 1634.
[15] H. Miguez, F. Meseguer, C. Lopez, M. Holgado, G. Andreasen, A. Mifsud, V. Fornes, Langmuir 16 (2000) 4405.
[16] B.T. Holland, C.F. Blanford, A. Stein, Science 281 (1998) 538.
[17] K. Yoshino, Y. Kawagashi, S. Tatsuhara, H. Kajii, S. Lee, A. Fujii, M. Ozaki, A.A. Zakhidov, Z.V. Vardeny, M. Ishikawa, Microelectron. Eng. (1999) 47.
[18] J.Q. Qi, Y. Wang, W.P. Chen, L.T. Li, L. Helen, W. Chan, J. Solid State Chem. 178 (2005) 279.
[19] Y.L. Zhang, Z.T. Kang, J. Dong, H. Abernathy, M.L. Liu, J. Solid State Chem. 179 (2006) 1733.
[20] C. Dujardin, C. Pedrini, W. Blanc, J.C. Gâcon, J.C. Vant Spijker, O.W. Vrijns, C.W.E. van Eijk, P. Dorenbos, R. Chen, A. Fremout, F. Tallouf, S. Tavernier, P. Bruyndonckx, A.G. Perosyan, J. Phys. Condens. Matter 10 (1998) 3061.
[21] M.A. Garcîa, J. Llopis, M.A. Villegas, S.E. Paje, J. Alloys Compds. 367 (2001) 323.
[22] X. Hu, Y. Wang, Y. Liu, B. Cheng, D. Zhang, Opt. Commun. 237 (2004) 371.
[23] J.F. Carvalho, A.C. Hernandes, Cryst. Res. Technol. 2005 (40) 847.
[24] C.E. Reese, C.D. Guerrero, J.M. Weissman, K. Lee, S.A. Asher, J. Colloid Interface Sci. 232 (2000) 76.
[25] P. Jiang, J.F. Bertone, K.S. Hwang, V.L. Colvin, Chem. Mater. 11 (1999) 2132.
[26] N.D. Denkov, O.D. Velev, P.A. Kralchevsky, I.B. Ivanov, H. Yoshimura, K. Nagayama, Nature 361 (1993) 26.
[27] H. Rietveld, J. Appl. Crystallogr. 2 (1969) 65.
[28] MS modeling release 3.0, Accelrys Inc., 9685 Scranton Road, San Diego, CA, USA, 2003 〈www.accelrys.com〉.
[29] T. Sen, G.J.T. Tiddy, J.L. Casci, M.W. Anderson, Chem. Mater. 16 (2004) 2044.
[30] H. Míguez, F. Meseguer, C. López, Á. Blanco, J.S. Moya, J. Requena, A. Mifsud, V. Fornés, Adv. Mater. 10 (1998) 480.
[31] L.S. Kasten, J.T. Grant, N. Grebasch, N. Voevodin, F.E. Arnold, M.S. Donley, Surf. Coat Technol. 140 (2001) 11.
[32] D. Makovec, Z. Samardžija, D. Kolar, J. Solid State Chem. 123 (1996) 30.
[33] M. DabalaÁ, L. Armelao, A. Buchberger, I. Calliari, Appl. Surf. Sci. 172 (2001) 312.
[34] R.H. Buttner, E.M. Maslen, Acta Crystallogr. B 48 (1992) 764.
[35] J.D. Bak, J.C. Wright, J. Phys. Chem. B 109 (2005) 18391.
[36] T.D. Dunbar, W.L. Warren, B.A. Tuttle, C.A. Randall, Y. Tsur, J. Phys. Chem. B 108 (2004) 908.